

Measurement of ocean wave height and direction by means of HF radar: an empirical approach

H.-H. ESSEN, K.-W. GURGEL, T. SCHLICK

Institut für Meereskunde, Universität Hamburg
Tropelwitzstr. 7, D-22529 Hamburg, Germany

Abstract

High-frequency (HF) radars have been used since 20 years for remotely sensing ocean surface currents and ocean waves. Backscattered Doppler spectra contain two discrete lines, the frequencies of which (Bragg frequency) determine the current speed, and four continuous side bands, which allow to apply inversion techniques for retrieving ocean wave spectra. Recently, a new HF radar has been developed at the University of Hamburg (Germany). Data of a 34-days experiment reveal a high correlation between the standard deviation of the Bragg frequencies and the significant wave height weighted by an azimuthal function. Applying empirical regression curves it is possible to determine the significant wave height and the mean wave direction from intersecting beams of two radar stations. Compared with inversion techniques the new method is applicable to data with lower signal-to-noise ratio, i.e. allows larger ranges. For current measurements, two radar sites are necessary. The optimum distance between two 30 MHz radars is about 20 km and, with the new method, needs not to be reduced for the purpose of simultaneous wave measurements.

Zusammenfassung

Seit 20 Jahren werden Hochfrequenz(HF)-Radarsysteme eingesetzt, um von der Küste aus Oberflächenströmungen und Seegang zu messen. Das rückgestreute Dopplerspektrum besteht aus zwei diskreten Linien, aus deren Frequenz (Braggfrequenz) die Strömung bestimmt wird, und aus vier kontinuierlichen Seitenbändern, aus denen mit Inversionsmethoden das Seegangsspektrum berechnet werden kann. An der Universität Hamburg wurde in den vergangenen Jahren ein neues HF-Radar entwickelt. Messungen über 34 Tage zeigen eine hohe Korrelation zwischen den Standardabweichungen der Braggfrequenz und der mit einer Richtungsfunktion gewichteten signifikanten Wellenhöhe. Mit Hilfe von empirischen Regressionskurven ist es möglich, die signifikante Wellenhöhe und die mittlere Wellenrichtung aus den Messungen zweier Radarstationen zu bestimmen. Im Vergleich zu den Inversionsmethoden ist das neue Verfahren bei geringerem Signal-zu-Rauschverhältnis

anwendbar, d.h. es erlaubt größere Reichweiten. Für Strömungsmessungen sind zwei Radarstationen erforderlich, deren optimaler Abstand für 30 MHz bei etwa 20 km liegt. Bei Anwendung des neuen Algorithmus muß dieser Abstand nicht reduziert werden, wenn gleichzeitig der Seegang gemessen werden soll.

1 Introduction

The high-frequency (HF) band covers frequencies between 3 and 30 MHz with wavelengths between 100 and 10 m. HF remote sensing is based on sky-wave or ground-wave propagation. This paper deals with ground-wave propagation only, and with radars operating from fixed positions at the coast. Parts of the transmitted HF power (ground wave) propagate along the sea surface following the Earth's curvature beyond the horizon. However, the working range is limited. Ground-wave attenuation increases with increasing HF frequency and decreasing surface-water conductivity (Gurgel et al., 1999a).

HF remote sensing is based on the scattering of electromagnetic waves from the rough sea surface. The basic physics were discovered and described by Crombie (1955). In the case of a monostatic configuration, i.e. transmitter and receiver at the same position, first-order Bragg scattering is due to ocean waves of half of the radar wavelength travelling towards or away from the radar site. Thus, the Doppler spectrum of the backscattered HF signal contains two discrete lines, the frequencies of which are determined by the phase velocity of the scattering ocean waves and the velocity of the underlying current. The first HF remote sensing system was the Coastal Ocean Dynamics Applications Radar (CODAR) of Barrick et al. (1977), which uses the first-order peaks for measuring ocean surface currents.

Hasselmann (1971) proposed the concept of second-order hydrodynamic and electromagnetic interaction giving rise to continuous second-order side bands in addition to two discrete first-order Doppler lines. He suggested that the second-order side bands around each first-order peak ought to be proportional to the frequency wave height spectrum. Thus, the integral of the normalized side bands should determine the significant wave height. Barrick (1972) derived a transfer function which relates the second-order radar cross section to the two-dimensional wave height spectrum of ocean surface waves. The theory is based on a perturbation expansion and the assumption that the sea surface is a perfect conductor. By making use of his theory, Barrick (1977) showed that, under certain conditions, the second-order side bands are proportional to the wave frequency spectrum multiplied by a weighting function.

In principal, the theory of Barrick (1972) allows to estimate the two-dimensional wave

height spectrum by inverting a nonlinear integral equation. This problem has been studied by a number of authors, e.g. Lipa (1978), Wyatt (1991), Howell and Walsh (1993), Hisaki (1996), and de Valk et al. (1999). By comparison with buoy data, Wyatt et al. (1999) found that the inversion procedure reveals a useful accuracy. The authors conclude that this method has a good potential for operational coastal monitoring.

The work with HF radar systems at the University of Hamburg dates back to 1981. A modified CODAR system has been operated in 15 field experiments, e.g. Essen et al. (1988), and Essen (1993). This system is designed for current measurements only. Recently, a new HF radar, called Wellen Radar (WERA), has been developed (Gurgel et al., 1999b). WERA transmits frequency-modulated continuous wave (FMCW) chirps instead of the continuous wave (CW) pulses of CODAR. One main advantage of the system is the possibility of connecting different configurations of receive antennas. When operated with a linear array, information on the sea state can be obtained.

Differently from the theoretical approaches mentioned, the method presented here is based on empirical results. Doppler frequencies used for determining the current velocities are found by averaging over a selected frequency band in the backscattered HF Doppler spectrum. The accompanying standard deviations are highly correlated with the significant wave height. This result refers to some 1500 simultaneous WERA and buoy measurements during 34 days of highly variable sea state.

The new WERA will be operated during experiments of the European Radar Ocean Sensing (EuroROSE) project, funded by the European Union. The project aims in predicting, for a few hours, off-shore currents and waves in coastal areas of high ship traffic. The predictions are based on in-situ measurements, included HF remote sensing. By making use of the algorithm presented here, wave height and direction will be estimated on the grid of current measurements. In addition, the inversion method of Wyatt (1991) will be applied.

Chapter 2 of this paper contains a short discussion of the theoretical background of wave measurement by HF radar. Beside the first- and second-order Bragg theory the composite-wave model is used to estimate the hydrodynamic modulation due to long waves which, by their orbital motion, induce an additional Doppler shift. After presenting some details about the WERA system and the experiment (Chapter 3), results are presented (Chapter 4). These include the estimation of significant wave height and wave direction from the radar measurements and in addition, the estimation of the wind direction.

2 Theory

Ocean surface waves are assumed to be a homogeneous random process. They are described by the two-dimensional wave height spectrum F ,

$$\langle \zeta^2 \rangle = \int F(\mathbf{k}) d\mathbf{k}, \quad (1)$$

where ζ is the wave height and \mathbf{k} the horizontal wavevector. The angle brackets denote ensemble means. This spectrum may be represented by its dependence on circular frequency ω and direction φ ,

$$F(\mathbf{k}) = \frac{1}{k} \frac{d\omega}{dk} E(\omega) S(\omega, \varphi), \quad (2)$$

$$\int E(\omega) d\omega = \langle \zeta^2 \rangle, \quad \int S(\omega, \varphi) d\varphi = 1,$$

with $\mathbf{k} = (k \sin \varphi, k \cos \varphi)$. The wavenumber k and the circular frequency ω are connected by the deep-water dispersion relation,

$$\omega^2 = gk, \quad (3)$$

where g is the gravity acceleration.

HF waves are transmitted parallel to the sea floor, i.e. at grazing incidence. Backscattering is well described by the Bragg theory. To the first order the backscatter is due to ocean waves of half of the radar wavelength travelling towards or away from the radar site (Bragg waves),

$$\mathbf{k}_B = \pm 2\mathbf{k}_0, \quad k_0 = \frac{\omega_0}{c}, \quad (4)$$

where the wavenumber k_0 is the modulus of the horizontal HF wavevector \mathbf{k}_0 , ω_0 the HF transmit circular frequency, and c the speed of light.

The moving Bragg waves induce a Doppler shift to the backscattered HF signal,

$$\omega_d = \pm \omega_B - 2\mathbf{k}_0 \mathbf{u}, \quad (5)$$

where ω_B is related to the wavenumber k_B by the dispersion relation, Eq. (3). The sign in front of ω_B depends on the direction of the scattering Bragg wave relative to the radar. The first term in Eq. (5) is due to the phase velocity of the Bragg waves and the second term due to the underlying current. The capability of an HF radar of measuring the radial component of surface current velocity is based on Eq. (5).

First-order Bragg theory predicts a Doppler spectrum consisting of two discrete lines. Second-order contributions are continuous. In the case that the main variance of the ocean wave height spectrum is concentrated at wavelengths which are much longer than the Bragg wave, the second-order Doppler spectrum becomes, cf. Hasselmann (1971),

$$D(\omega_D) = F(\mathbf{k}_B) \int T(\Omega, \varphi) E(\Omega) S(\Omega, \varphi) d\varphi, \quad \omega_D = \pm\omega_B \pm \Omega, \quad (6)$$

with Ω being the circular frequency of the long surface waves, and T a theoretically known transfer function. Thus, two second-order Doppler spectra fold around each of the two Bragg lines.

Eq. (6) has been used by several authors for retrieving ocean-wave spectra by means of inversion methods, e.g. Wyatt (1991). The transfer function T used is that of Barrick (1972) which accounts for both electromagnetic and hydrodynamic interactions. However with respect to applications, the theory contains two shortcomings: 1) A perfectly conducting sea surface has to be assumed in order to obtain nonvanishing backscatter. 2) The theory relies on a perturbation expansion assuming that the height of ocean waves is small compared with the HF wavelength. Including long waves, which generate the second-order side bands, this assumption often fails.

The Bragg theory assumes that surface currents are stationary during the measuring time of e.g. 10 min. However, orbital motions of long waves (carrying the short Bragg waves) induce a Doppler shift which varies during the measuring periods. Thus, long waves cause a broadening of the first-order Doppler spectrum. The effect is estimated by means of the composite wave model, cf. Wright (1978). The model assumes that the wavelengths of the modulating surface waves are much longer than those of the scattering Bragg waves. The long waves are locally approximated by plane facets. The facets move with the orbital motion of the long waves and induce an additional Doppler shift (hydrodynamic modulation). Our approach does not account for the slopes of the facets (tilt modulation).

HF measurements perform both averaging in space (due to the pulse length) and time (due to the measuring time). The orbital velocity can be considered as random variable with zero mean and normal probability distribution. Because of the linear dependence on the orbital velocity, Eq. (5), ω_d is normally distributed with mean m and variance σ^2 ,

$$m = \langle \omega_d \rangle = \pm\omega_B - 2k_0 U_x, \quad \sigma^2 = \langle (\omega_d - m)^2 \rangle = 4k_0^2 \langle u_x^2 \rangle, \quad (7)$$

where, for simplicity, it is assumed that the radar wavevector \mathbf{k}_0 points into the direction of the x-axis. U_x is the radial velocity component of the underlying homogeneous and

stationary current, and u_x the radial component of the orbital velocity of the long ocean waves.

The orbital velocity \mathbf{u} of ocean surface waves depends on the wave height ζ by,

$$\frac{\partial \mathbf{u}}{\partial t} = -g \frac{\partial \zeta}{\partial \mathbf{x}}. \quad (8)$$

This equation determines the variance of the orbital velocity component u_x in terms of the two-dimensional wave height spectrum,

$$\langle u_x^2 \rangle = g \int \frac{K_x^2}{K} F(\mathbf{K}) d\mathbf{K}, \quad (9)$$

where the capital \mathbf{K} indicates that the integration refers to the modulating long waves.

Second-order Bragg scattering and hydrodynamic modulation contribute to the broadening of the HF Doppler spectrum which, for both mechanisms, increases with increasing sea state. In general, the two effects can not be separated, cf. Esssen et al. (2000). The observed broadening can be quantified in terms the standard deviation which is found to be strongly correlated with the significant wave height.

3 Data

The data presented here are from the Surface Current and Wave Variability Experiments (SCAWVEX) which were funded by the European Union. The primary objective of SCAWVEX was to provide data sets that measure the spatial and temporal variability of ocean surface waves and currents. Three experiments were carried out between fall 1994 and fall 1996: 1) Holderness, England, 2) Maasmond, Netherlands, 3) Petten, Netherlands. Another objective of SCAWVEX was to develop and to test a new HF radar, called Weller Radar (WERA). WERA was operated during the Maasmond experiment for a short test period, but continuously during the Petten experiment.

The main aim of the Petten experiment was to demonstrate the capability of WERA for measuring waves. The experiment was held from 29 October to 7 December 1996 in the north-western part of the Netherlands near to the town Petten. The measuring area is about 100 km north of the Rhine mouth. Fig. 1 shows the location of the experiment and the positions of the instruments referred to in this paper.

The WERA sites are marked by R1 and R2 in Fig. 1. In order to realize a high signal-to-noise ratio at positions where both radar beams intersect, the radar sites were

deployed only 10 km apart (base line). The high signal-to-noise ratio is needed for resolving the second-order side bands which are used to retrieve wave information by inversion techniques. However, it will be shown later that this configuration is not optimum for the method described here.

A detailed description of the WERA system is given by Gurgel et al. (1999b). During the Petten experiment the WERA was operated at 27.65 MHz. The corresponding Bragg frequency ($\omega_B/2\pi$) and wavelength ($2\pi/k_B$) are 0.54 Hz and 5.4 m, respectively. WERA transmitted linear frequency chirps of 0.26 s duration (sampling rate). The frequency shift between the transmitted and received signal determines the range. The complex Fourier amplitudes of the received chirp represent the samples of the slowly varying time series at different ranges. The range cell depth is determined by the bandwidth of the chirp. A range resolution of 1.2 km was chosen and reduced to 0.3 km for the last two days of the experiment. The high resolution data are not considered here, i.e. in the context of wave measurement.

Both WERA sites were operated with a 16-element receive array, and beam-forming was applied for azimuthal resolution. The resolution of the antenna array is about $\pm 3^\circ$. The measuring period was 9 min (2048 samples). In order to avoid interference, the two sites were operated successively, and repeated every 20 min. The time series recorded by the radars are divided into 50 % overlapping subseries of 512 samples. The Doppler spectra of the subseries are averaged, in order to increase the statistical significance. Depending on the sea condition maximum ranges varied between 30 and 50 km. The ranges mentioned refer to current measurements. The identification of second-order side bands, i.e. the determination of wave spectra by inversion techniques, is only possible to about half these ranges.

Fig. 2 displays two Doppler spectra measured by the WERA at position R2 in Fig. 1, one recorded during low sea state the other during high state. Unfortunately, the radar at Petten (R1) suffered from radio interference with the wave buoys. The wave buoys worked like transponders by receiving the radar signal, modulating and retransmitting it. Distortions of parts of the chirp signal lead to noisy data at a range of about 20 km.

The directional waverider at position D in Fig. 1 measures, in terms of frequency, the spectral density of the wave height, the mean direction and the spreading of the azimuthal distribution. Fig. 3 presents an example. The significant wave height, obtained from the sum of the spectral amplitudes, is 3.5 m. Time series of the significant wave height and the mean wave direction are displayed in the upper two panels of Fig. 4. The mean wave directions are shown for the peak frequency of the spectrum and the shortest wavelength measured by the buoy which is 6.2 m and somewhat longer than the Bragg wavelength of 5.4 m.

During the 34-days measuring time the significant wave height varied strongly between values less than 0.5 m and higher than 4 m. There is a general correlation with the wind speed which however, is not perfect. The difference may be due to the different locations of wind and wave measurement (cf. Fig. 1) or due to longer waves which are not generated locally. The latter assumption is confirmed by deviations of wind direction from the mean wave direction of the peak frequency. Better agreement is found for the mean direction of short waves which is represented by the dotted line in Fig. 4 (second panel).

4 Results

The amplitudes of the two first-order Bragg lines have been used by several authors to determine the mean direction of the Bragg waves, e.g. Heron (1987), and Wyatt et al. (1997). These short waves are generated by the local wind. Thus, it can be assumed that their direction coincides with the wind direction. This concept is tested with the Petten data in the first part of this chapter. The second part investigates the standard deviation of the Bragg frequencies and its connection with the sea state.

4.1 Wind direction

The first-order Doppler spectrum consists of two discrete lines and can be represented as,

$$D(\omega) \sim E(\omega_B)[S(\varphi_r)\delta(\omega - \omega_{dp}) + S(\varphi_r + \pi)\delta(\omega + \omega_{dm})] \quad (10)$$

where φ_r is the azimuthal direction of the radar beam. The indices p and m of ω_d refer to the plus- and minus-sign in Eq. (5), respectively. Due to underlying currents the Doppler frequencies are slightly different from the Bragg frequencies, cf. Eq. (5). However, their distance is independent of the current,

$$\omega_{dp} - \omega_{dm} = 2\omega_B. \quad (11)$$

In general, the first-order peaks extend over several spectral lines. This is due to the Fourier decomposition applied but also to the influence of underlying long waves which induce an additional Doppler shift (cf. Chapter 3). The processing method applied searches for the two spectral peaks in the vicinity of the Bragg lines. Then averaging is performed over a certain interval around the peaks. The two peak frequencies are determined by weighting the frequencies with the signal strength (=squared Fourier amplitude). A quality check is performed. If the distance of the two peak frequencies deviates by more than 2 % from $2\omega_B$, cf. Eq. (11), the data are discarded.

In order to retrieve the wave direction, a model for the angular distribution of the short scattering ocean waves has to be considered, e.g.,

$$S(\varphi) = A_s \cos^s[0.5(\varphi - \varphi_0)] \quad (12)$$

where φ_0 is the mean wave direction, and s describes the azimuthal spreading. A_s is a normalisation constant determined by Eq. (2). By means of Eq. (10) the quotient of the spectral densities of the two Doppler lines becomes,

$$r = \frac{\cos^s[0.5(\varphi_r + \pi - \varphi_0)]}{\cos^s[0.5(\varphi_r - \varphi_0)]}, \quad (13)$$

where φ_r is the look direction of the radar. Considering a special exponent, e.g. $s = 4$, Eq. (13) allows to determine φ_0 , however with a left-right ambiguity relative to φ_r . With two radars viewing a surface pixel from different azimuths, Eq. (13) allows the computation of both the mean direction φ_0 and the azimuthal spreading s .

The method described is applied to the position D of the waverider buoy in Fig. 1. The location is at a distance of about 10 km from both radar sites. There, the area illuminated by the radars is about 1 km² due to the beam width of 6° and the range resolution of 1.2 km. Fig. 5 compares the mean directions derived from the radar with those measured by the directional wave rider and with the wind direction. The Bragg wavelength (5.4 m) and the shortest wavelength resolved by the buoy (6.2 m) differ slightly. The 1-hourly sampled time series contains 816 data. Only 23 WERA data pairs, i.e. less than 3 % do not allow to identify the two Bragg lines for both radar sites. Thus, there are nearly always 5-m waves travelling in opposite directions.

The overall agreement of the time series of Fig. 5 is good. However, the rms differences are relatively high, 39° between radar and buoy direction, 39° between radar and wind direction, and 42° between buoy and wind direction. There are several possible reasons for this finding. Single radar measurements may be perturbed by interference with remote radio stations or reflections from ships. The buoy measurements at the shortest wavelength resolved are very noisy, and the wave direction may deviate from the instantaneous wind direction.

In principal, Eq. (13) allows to determine the spreading of the angular distribution and, except for a constant factor, the spectral density at the Bragg wavelength. The spreading of both the buoy and the radar measurements vary between 40° and 70° in an almost random manner. Except for the order-of-magnitude there is little agreement in detail. The same applies to the spectral density. The noise can partly be attributed to the radar but also to the buoy measurements.

Wyatt et al. (1997) developed a more sophisticated method for retrieving the wave direction. The method is based on the maximum-likelihood method applied to the overlapping partial time series mentioned before. Others than the azimuthal function, Eq. (12), were tested. Comparisons of the Petten WERA and buoy data are presented by Wyatt et al. (1999) and reveal about the same agreement as Fig. 5.

4.2 Wave height and direction

The standard deviation of the two Bragg lines is computed by averaging over a broader interval than used for the determination of the first-order Bragg lines, i.e. the current speed. However, the method is the same. The Doppler shifts are weighted by their signal strengths. The standard deviations are computed for both Bragg lines,

$$\sigma_p = \langle (\omega - \omega_{dp})^2 \rangle, \quad \sigma_m = \langle (\omega - \omega_{dm})^2 \rangle \quad (14)$$

In general, the averaging accounts for both second-order Bragg scattering and orbital motion of long waves (hydrodynamic modulation), cf. Chapter 3. At ranges less than about 15 km the HF Doppler spectra reveal clearly visible second-order side bands. The contribution of hydrodynamic modulation is less than predicted by theory, cf. Essen et al. (2000). Most probably this is due to the fact that the main assumption of the composite wave model is violated. The facets should be by one order larger than the Bragg wave, and the long waves by one order larger than the facets, i.e. the long waves by two orders larger than the Bragg wave.

Correlations of the standard deviations, defined by Eq. (14), with different sea-state functions have been computed. The highest correlation was found for the total variance composed from both Bragg lines (σ) and the significant wave height weighted by a \cos^2 azimuthal function (h_φ),

$$\sigma = \sqrt{\frac{s_p \sigma_p^2 + s_m \sigma_m^2}{s_p + s_m}}, \quad (15)$$

$$h_\varphi = h_s \cos^2[0.5(\varphi_r - \varphi_0)], \quad (16)$$

where s_p and s_m are the cumulative signal strengths of the first-order Bragg lines. h_s is the significant wave height, φ_0 the mean direction at the peak frequency and φ_r the azimuthal direction of the radar beam. Fig. 6 displays the time series σ from both radar stations and the respective sea-state series h_φ measured by the buoy. Despite the noise in both the buoy and the radar data the correlations are high.

The high correlation allows to assume a linear relationship between the quantities defined by Eqs. (15) and (16),

$$h_\varphi = \alpha + \beta\sigma. \quad (17)$$

The regression coefficients found for the two radar sites are about the same (see below). They are used to retrieve the significant wave height h_s and the mean direction φ_0 from the Doppler standard deviations as measured at the two WERA sites,

$$h_s \cos^2[0.5(\varphi_i - \varphi_0)] = \alpha_i + \beta_i\sigma_i = X_i, \quad (i = 1, 2), \quad (18)$$

with φ_i being the azimuthal beam direction of the radar site i at a given position on the sea surface.

The solution of Eq. (18) is not unique, there exist two φ_0 and corresponding h_s for a measurement (X_1, X_2) . One angle is in the circular segment defined by the lines connecting the illuminated area with the two radar sites, the other angle is in the remaining segment. For the data under investigation, the waves are propagating more or less towards the coast. For this reason, there arises no problem in finding the correct angle. In most coastal applications the situation will be similar. Otherwise additional information on the mean wave direction is needed.

Fig. 7 displays the significant wave height and the mean wave direction as measured by the buoy and retrieved from the radar data. The upper panel shows all data available. In general, the wave heights agree well. However, the radar data contain some noise. Most probably the noise is due to sources like reflection from ships or radio interference. By inspecting the noisy data, it was found that they are related to high values of,

$$q = 10|\log X_2 - \log X_1|. \quad (19)$$

Discarding measurements with $q > 3$ about 15 % of the data get lost but the radar time series lose most of the noise, cf. Fig. 7 (middle panel). Noise remains in the time series of mean wave direction, mainly during periods of low sea state with a significant wave height less than 1 m.

Wyatt et al. (1999) applied the inversion technique to the Petten data. The agreement of the retrieved significant wave height with the buoy measurement is about the same as in Fig. 7. While the inversion technique shows a trend of overestimating high sea states by the radar, the opposite is the case for the empirical method. The comparison of the mean wave direction reveals better results for the empirical method, i.e. more robust estimates for periods of low sea state.

An attempt was made, to improve the agreement of retrieved and measured wave heights, by considering a quadratic instead of a linear regression curve, i.e. determining

three instead of two regression coefficients. The correlation coefficients in Fig. 6 increased by less than 1 %. Somewhat higher wave heights were retrieved for the 6-November, i.e. a better agreement could be achieved. However, the regression coefficients of both radar sites differ. We want to apply the regression technique to other areas than the position of the buoy. For this reason, we confine ourselves to the more robust linear regression.

Fig. 8 describes the geometrical constraints of the Petten experiment. Grid points are indicated for which wave parameters will be computed. The dashed lines show the azimuthal $\pm 45^\circ$ sections within which beamforming allows a good angular resolution. The dotted circles represent positions where the beams of the two radars intersect by 90° , 60° and 30° , respectively. The dashed-dotted line indicates the range where the interference of the Petten WERA with the buoy is maximum. i.e. the data are of reduced quality.

Correlation and regression coefficients of the WERA standard deviation σ , measured at the grid points of Fig. 8, and the buoy-measured wave function h_φ , have been calculated, cf. Eqs. (15)-(18). Here we assume that, in the mean, the wave field is homogeneous in the area covered by the grid system. The total number of grid points is 30. Correlation coefficients higher than 0.8 have been found at 26 grid points for radar site R1 and at 27 grid points for radar site R2. The grid points with lower correlation are outside the azimuthal coverage indicated in Fig. 8. The number of grid points with correlation coefficients higher than 0.9 is 17 for site R1 and 21 for site R2. The reduced performance of R1 is due to the interference problem mentioned.

Considering grid points with correlation coefficients exceeding 0.9, the regression coefficients become,

$$\begin{aligned}\alpha_1 &= -0.45 \pm 0.07, & \beta_1 &= 44.2 \pm 1.1 & (R1), \\ \alpha_2 &= -0.48 \pm 0.08, & \beta_2 &= 44.0 \pm 1.1 & (R2).\end{aligned}\tag{20}$$

Thus, the regression coefficients are about the same for both radar sites and for different grid points. The error of the retrieved wave height due to the variability of the regression coefficients is of the order of 3 %. Considering, in addition, grid points with correlation coefficients between 0.8 and 0.9 the regression coefficients of radar site R2 are only slightly affected while those of radar site R1 reveal higher deviations.

Fig. 9 displays wave height and direction (= wavevector), as retrieved from the WERA measurements, on the grid of Fig. 8. The direction is that towards which the waves are propagating, i.e. deviates by 180° from the meteorological convention. The significant wave height measured by the buoy is 3.5 m. Applying the constant regression coefficients of Eq. (20), the retrieved wavevectors reveal, at some grid points, deviations from the buoy measurement at position D, mainly in direction. Better results are found by using regression coefficients computed separately for the single grid points. Grid points with

correlation coefficients higher than 0.9 for both radar sites show good agreement for both methods applied. Considering the restrictions with respect the geometry and to the interference problem with radar station R1, the result looks quite satisfactory. By extending the distance between the two radar sites from 10 km to 20 or 25 km, which is the normal configuration for current measurements, better results can be expected.

An example for a low sea state, with significant wave height of 0.7 m, is presented in Fig. 10. At some grid points the retrieved wave heights are considerably larger than that one measured by the buoy. However, these data fail the quality criterion, i.e. the quantity q in Eq. (19) exceeds a given threshold. These are mainly measurements taken at low sea states which fail the quality criterion. However, if this is the case for a certain grid point, adjacent grid points may yield reliable measurements, cf. Fig. 10. Thus, a mean wavevector can be estimated by averaging those wavevectors which fulfil quality criterion.

In order to investigate the ranges which can be realized by the method presented, time series of the standard deviations of the WERA measurements have been computed for different ranges and azimuths. Because of the interference problem with station R1, we rely on the data of station R2. It is found that up to distances of 30 km the time series reveal the same structures. At larger distances noise dominates. The grid in Fig. 8 extends to a distance of 24 km from shore. Because of the short distance between the WERA sites, the angle of intersection between the two radar beams becomes extremely disadvantageous at larger ranges, cf. Fig. 8.

5 Conclusions

An algorithm (= empirical method) is presented which allows to estimate significant wave height and mean wave direction in conjunction with HF surface current measurements. The processing of HF data provides the frequency (= Bragg frequency) of two peaks of the Doppler spectrum, which are used to estimate the surface current, and in addition, the standard deviation of the Bragg frequency. The empirical method is based on a high correlation between the standard deviation and the significant wave height weighted by an azimuthal function. The correlation refers to simultaneous HF and buoy measurements during a 34-days period of highly variable sea state. However, the empirical method is not capable of determining the spectral distribution of the wave energy.

Based on theoretical relations, inversion techniques are reported in the literature which allow to estimate the two-dimensional wave height spectrum from HF measurements. With respect to the significant wave height and the mean wave direction the performance is about the same as that of the empirical method, cf. Wyatt et al. (1999). However,

the inversion technique requires a high signal-to-noise ratio which, as compared to the empirical method, leads to a stronger limitation in range. When using intersecting beams of two radar sites, the inversion technique requires shorter distances between the sites than are optimum for current measurements and wave measurements relying on the empirical method. A further advantage of the empirical method is the simple performance, e.g. no normalisation of spectral side-bands is needed.

The attempt of determining the spatial variability of wave height and direction from the HF data was only partially successful. The method requires that, at the grid point under consideration, data of both radar stations yield about the same regression coefficients. This was not the case in the area where one of the radars was perturbed by radio interference. We expect that, with undisturbed data, the method can be applied to the EuroROSE experiments at the coasts of Norway and Spain in spring and fall 2000, respectively.

Acknowledgements

This work is part of the EuroROSE project, funded by the European Union (EU). The buoy data used were gathered during a SCAWVEX experiment (funded by EU) by Rijkswaterstaat (The Netherlands). Thanks go to our colleagues G. Antonischki, M. Hamann and F. Schirmer, who participated in the HF experiment.

References

- D. E. Barrick, "Remote sensing of the sea state by radar," In: Remote Sensing of the Troposphere (Ed. V. E. Derr). US Government Printing Office, Washington DC, Ch. 12, 1972.
- D. E. Barrick, M. W. Evans, B. L. Weber, "Ocean surface current mapped by radar," *Science*, vol. 198, pp. 138-144, 1977.
- D. E. Barrick, "Extraction of wave parameters from measured HF radar sea-echo Doppler spectra," *Radio Science*, vol. 12, pp. 415-425, 1977.
- D. D. Crombie, "Doppler spectrum of sea echo at 13.56 Mc/s," *Nature*, vol. 175, pp. 681-682, 1955.
- C. de Valk, A. Reniers, J. Atanga, A. Vizinho, J. Vogelsang, "Monitoring surface waves in coastal waters by integrating HF radar measurements and modelling," *Coastal Engineering*, vol. 37, pp. 431-453, 1999.

- H.-H. Essen, K.-W. Gurgel, F. Schirmer, "Horizontal and temporal variability of surface currents in the 'Lübecker Bucht', as measured by radar," *Dt. hydrogr. Z.*, vol. 41, pp. 57-74, 1988.
- H.-H. Essen, "Ekman portion of surface currents, as measured by radar in different areas," *Dt. hydrogr. Z.*, vol. 45, pp. 57-85, 1993.
- H.-H. Essen, K.-W. Gurgel, T. Schlick, "On the accuracy of current measurements by means of HF radar," *IEEE J. Oceanic Eng.*, in print, 2000.
- K.-W. Gurgel, H.-H. Essen, S. P. Kingsley, "High-frequency radars: physical limitations and recent developments," *Coastal Engineering*, vol. 37, pp. 201-218, 1999a.
- K.-W. Gurgel, G. Antonischki, H.-H. Essen, T. Schlick, "Wellen Radar (WERA): a new ground-wave HF radar for ocean remote sensing," *Coastal Engineering*, vol. 37, pp. 201-218, 1999b.
- K. Hasselmann, "Determination of ocean wave spectra from Doppler radio return from the sea surface," *Nature*, vol. 229, pp. 16-17, 1971.
- M. L. Heron, "Directional spreading of short wavelength fetch-limited wind waves," *J. Phys. Oceanogr.*, vol. 17, pp. 281-285, 1987.
- Y. Hisaki, "Nonlinear inversion of the integral equation to estimate ocean wave spectra from HF radar," *Radio Science*, vol. 31, pp. 25-39, 1996.
- R. Howell, J. Walsh, "Measurement of ocean wave spectra using narrow-beam HF radar," *IEEE J. Oceanic Eng.*, vol. 18, pp. 296-305, 1993.
- B. Lipa, "Inversion of second-order radar echos from the sea," *J. Geophys. Res.*, vol. 83, pp. 959-962, 1978.
- J. W. Wright, "Detection of ocean waves by microwave radar; the modulation of short gravity-capillary waves," *Boundary-Layer Met.*, vol. 13, pp. 87-105, 1978.
- L. R. Wyatt, "HF radar measurements of the ocean wave directional spectrum," *IEEE J. Oceanic Eng.*, vol. 16, pp. 163-169, 1991.
- L. R. Wyatt, L. J. Ledgard, W. Anderson. "Maximum-likelihood estimation of the directional distribution of 0.54-Hz ocean waves," *Journal of Atmospheric and Oceanic Technology*, vol. 14, pp. 591-603, 1997.

L. R. Wyatt, S. P. Thompson, R. R. Burton. "Evaluation of high frequency radar measurement," *Coastal Engineering*, vol. 37, pp. 259-282, 1999.

Figure captions

Figure 1: Coast of the Netherlands, and positions of the two WERA sites (R1,R2), the directional waverider buoy (D) and the wind sensor (W).

Figure 2: WERA Doppler spectra received from a range at a distance of 12 km in the main look direction of the antenna. The significant wave heights during the measurements were 0.7 m (left panel) and 3.5 m (right panel). The dB-scale refers to the maximum spectral amplitude. The dotted vertical lines indicate the Bragg frequencies.

Figure 3: Wave height spectrum, measured by the directional waverider buoy. The left panel shows the frequency spectrum, the right panel the mean direction (full line) and the spreading indicated by the two dashed lines.

Figure 4: Time series of waves and wind measured at position D and W in Fig. 1, respectively. Panels from above: 1) significant wave height, 2) mean wave direction at the peak frequency of the spectrum (full line) and at 6.2 m wavelength (dotted line), 3) windspeed, 4) wind direction. Meteorological convention is used for both wave and wind direction.

Figure 5: Time series of the mean Bragg wave direction retrieved from the radar (full lines), measured by the directional waverider at 6.2 m wavelength (upper panel, dotted line) and the direction of the wind (lower panel, dotted line). Meteorological convention is used for both wave and wind direction.

Figure 6: Total standard deviation σ as measured by WERA (full lines) and the sea-state function h_φ derived from buoy measurements (dotted lines), cf. Eqs. (15)-(16). The upper panel refers to WERA site R1, the lower to R2, cf. Fig. 1.

Figure 7: Comparison of significant wave height and mean wave direction as retrieved from the WERA standard deviations (full lines) and measured by the buoy (dotted lines). The upper panel displays all data available, the lower two panels only those data which fulfil the quality criterion of Eq. (19).

Figure 8: Grid system with 4 km spacing (crosses) and locations of instruments (R1, R2, D), cf. Fig. 1. Azimuthal coverage (dashed lines), circles of equal intersection by 30° , 60° and 90° (dotted circles) and range of data affected by interference (dashed-dotted circle) are indicated.

Figure 9: Wave height and direction measured by a buoy at position D and retrieved from WERA measurements on the grid of Fig. 8. The arrows indicate the wave direction,

their length is proportional to the wave height. Full arrows refer to regression coefficients computed separately for each grid point, dotted arrows refer to the constant regression coefficients of Eq. (20).

Figure 10: Wave height and direction measured by a buoy at position D and retrieved from WERA measurements on the grid of Fig. 8. The arrows indicate the wave direction, their length is proportional to the wave height. Dotted and dashed arrows fail the quality criterion $q < 3$ and $q < 2$, respectively, cf. Eq. (19).

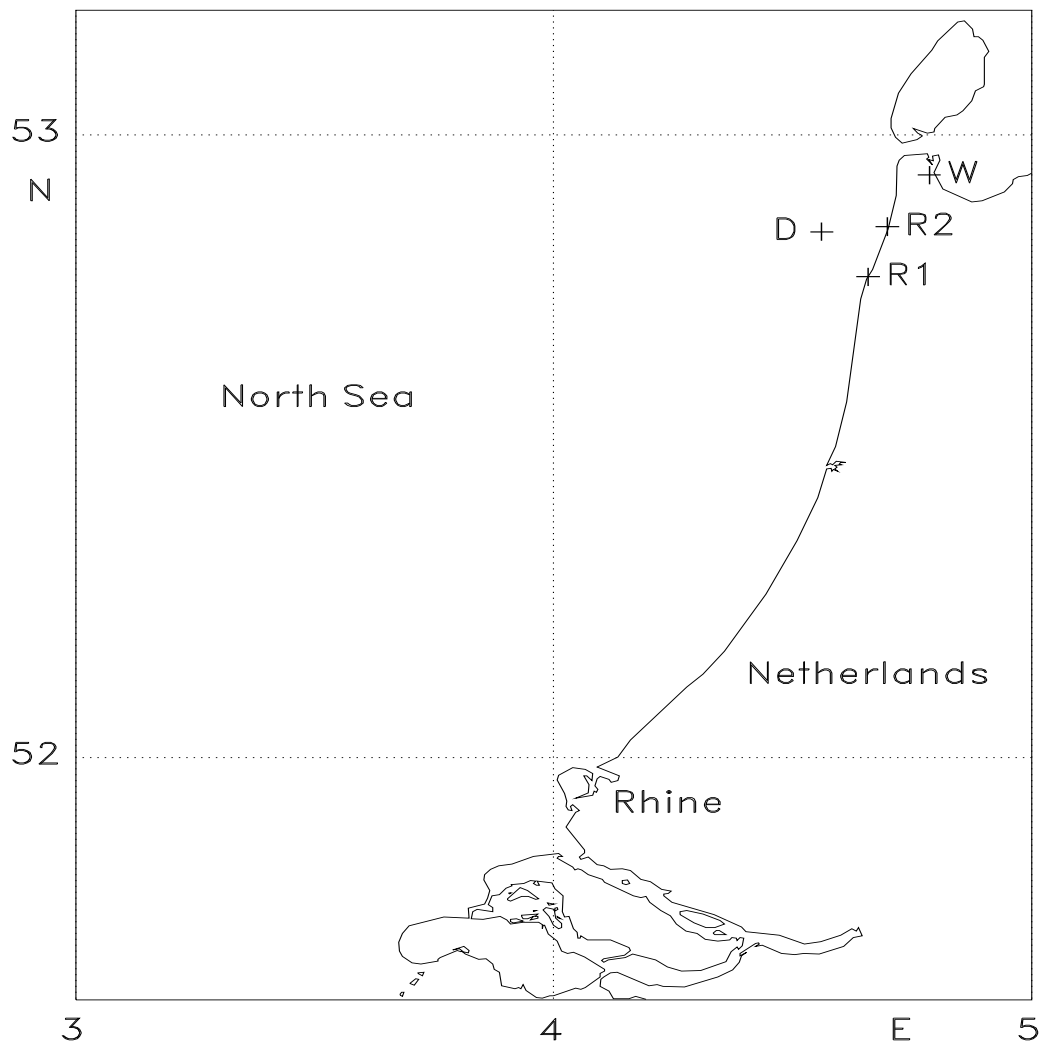


Figure 1

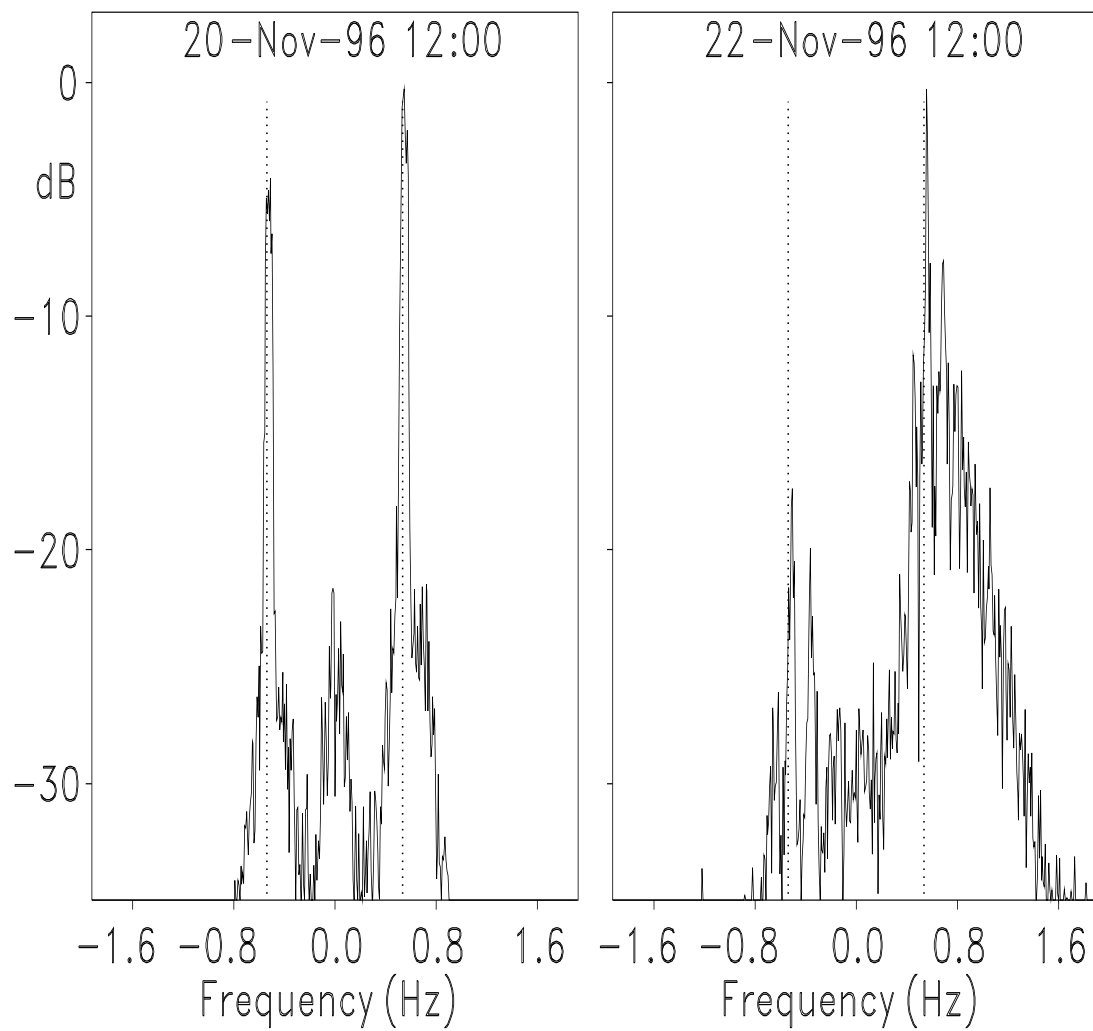


Figure 2

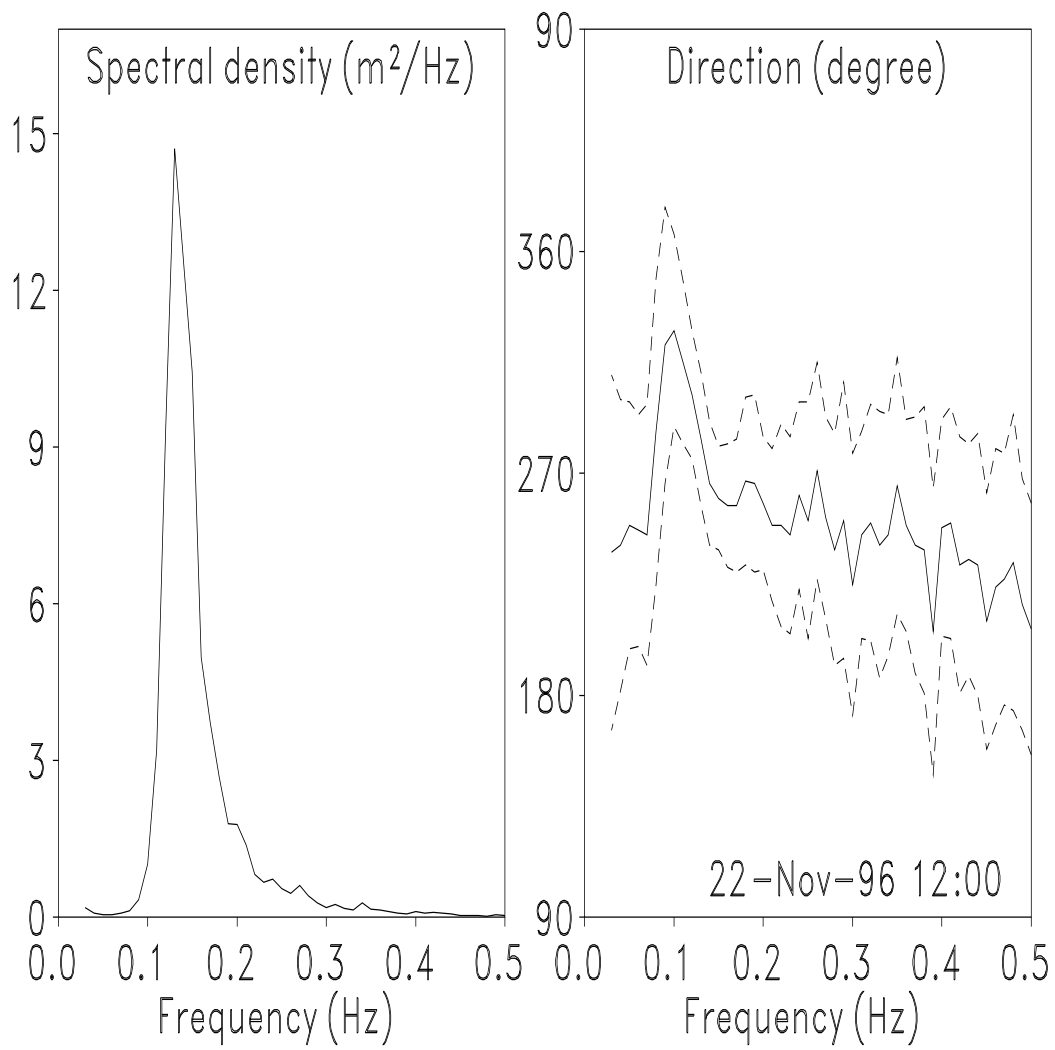


Figure 3

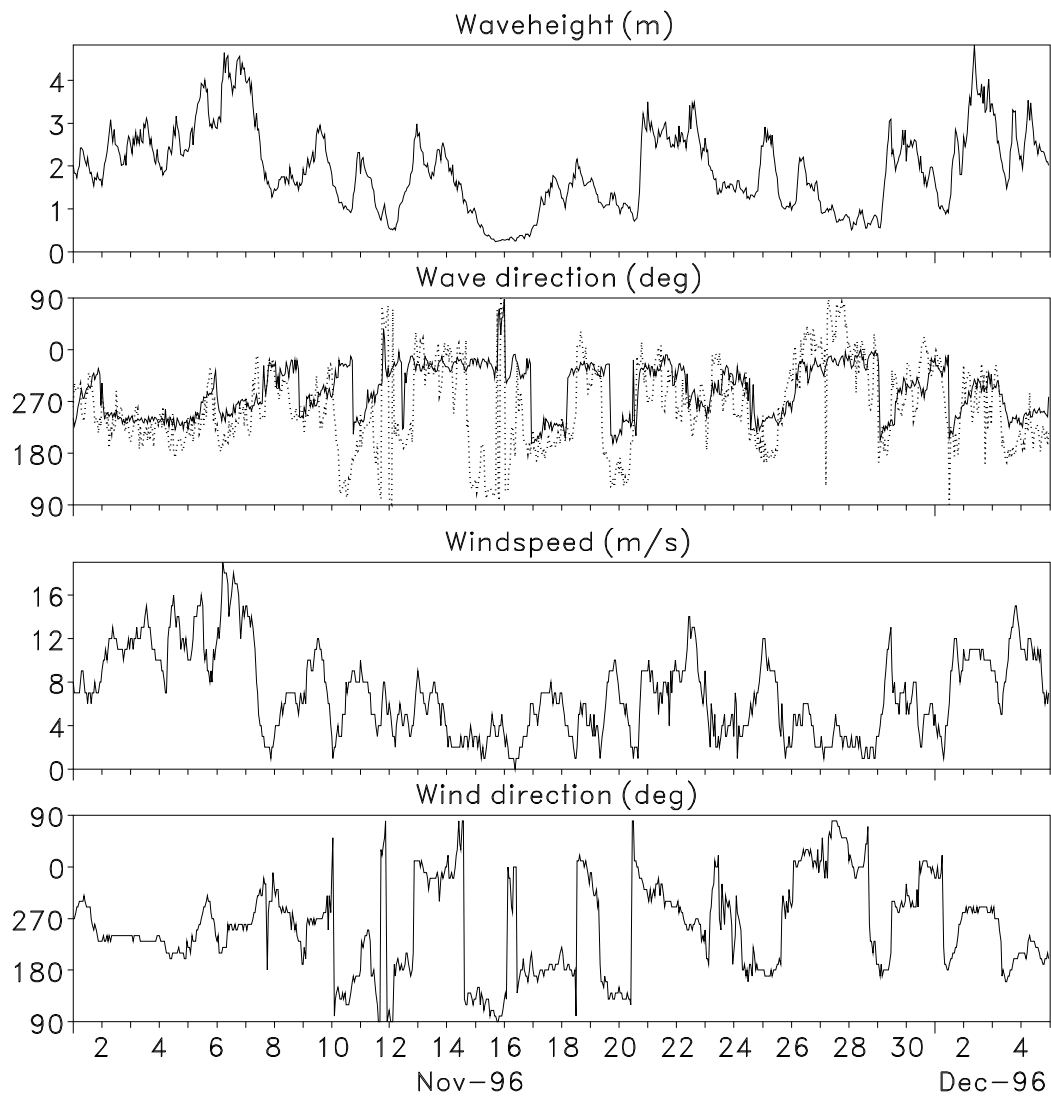


Figure 4

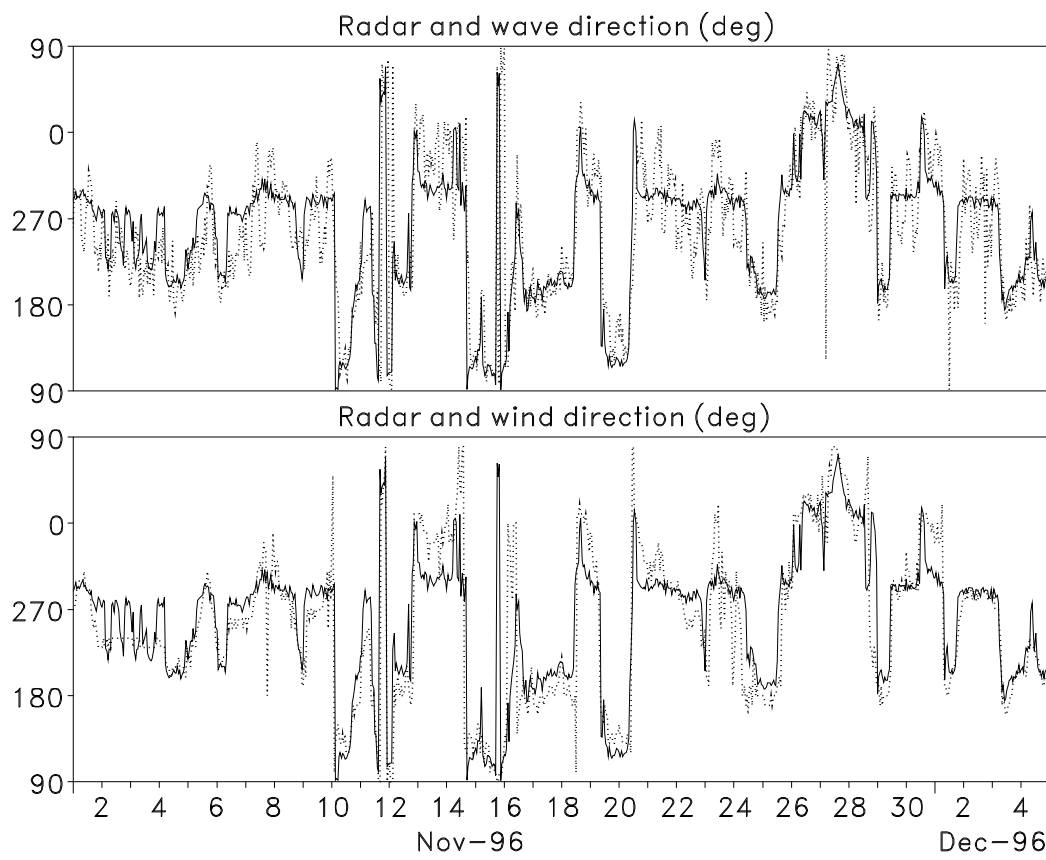


Figure 5

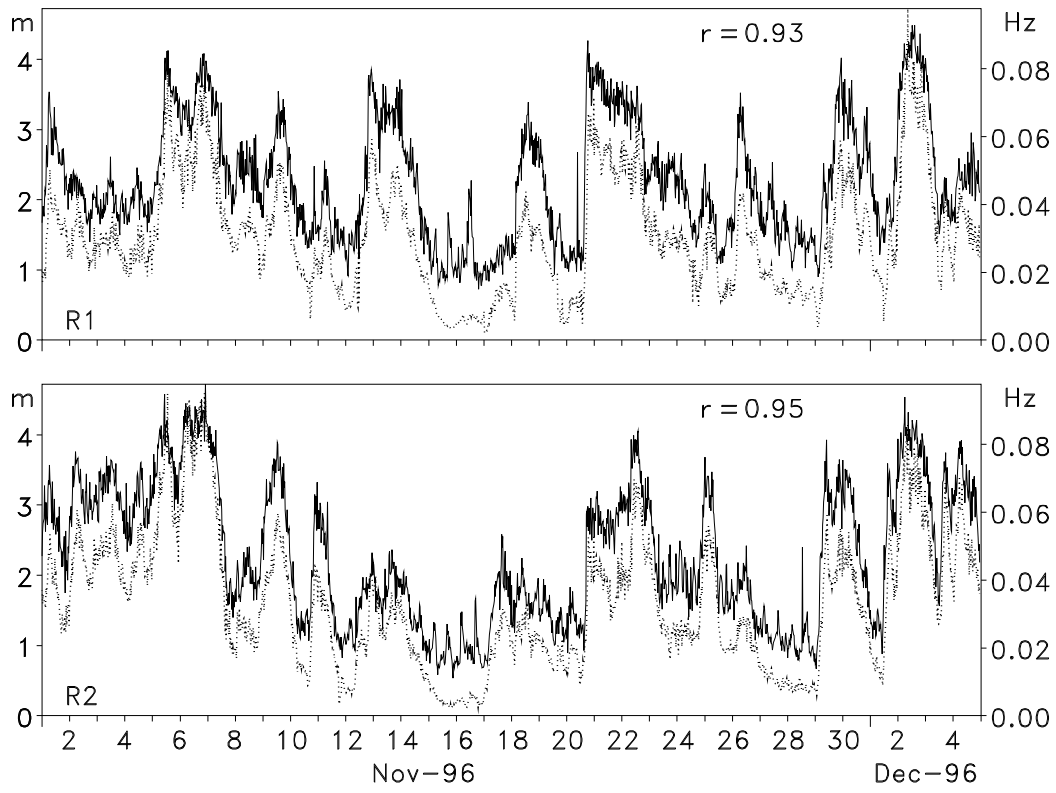


Figure 6

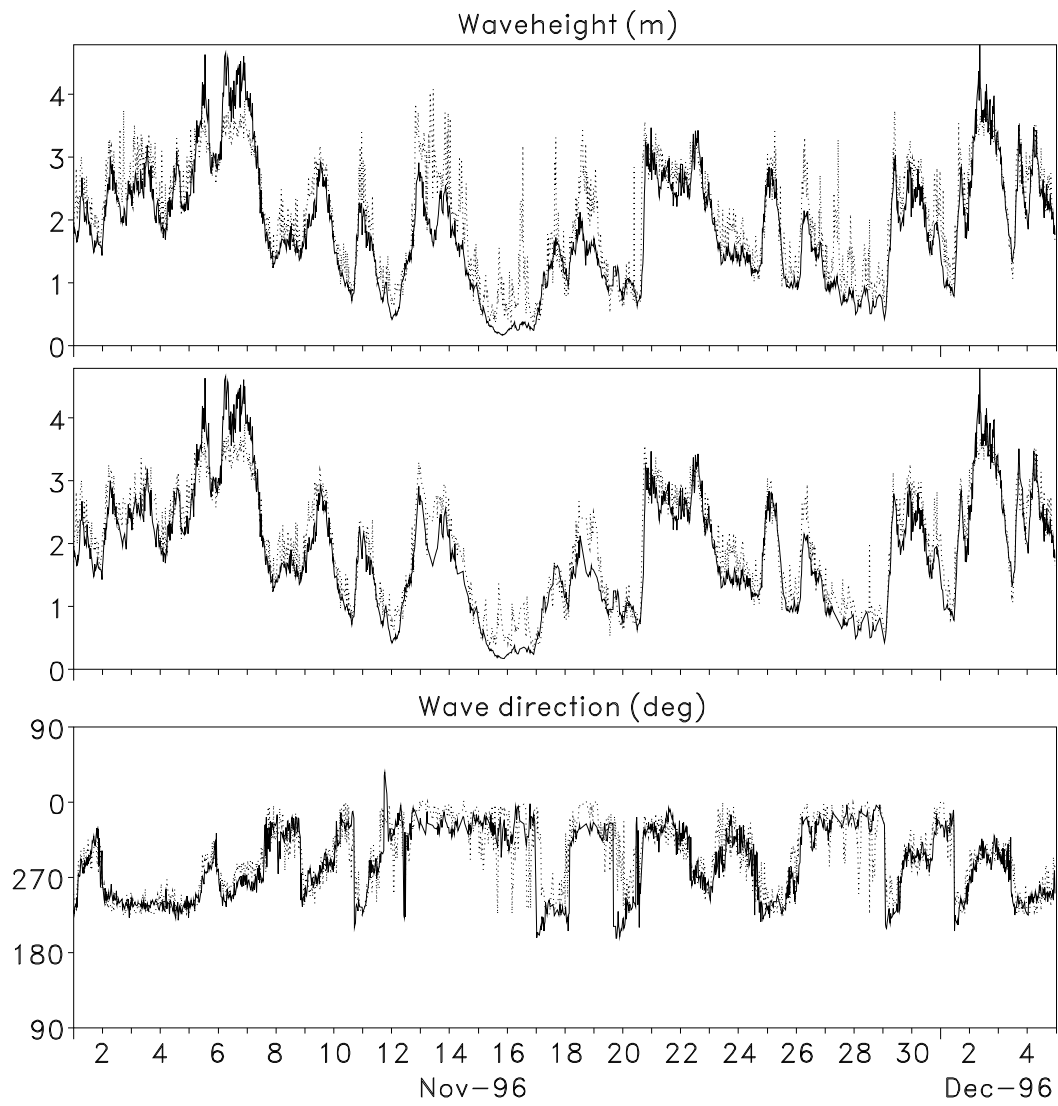


Figure 7

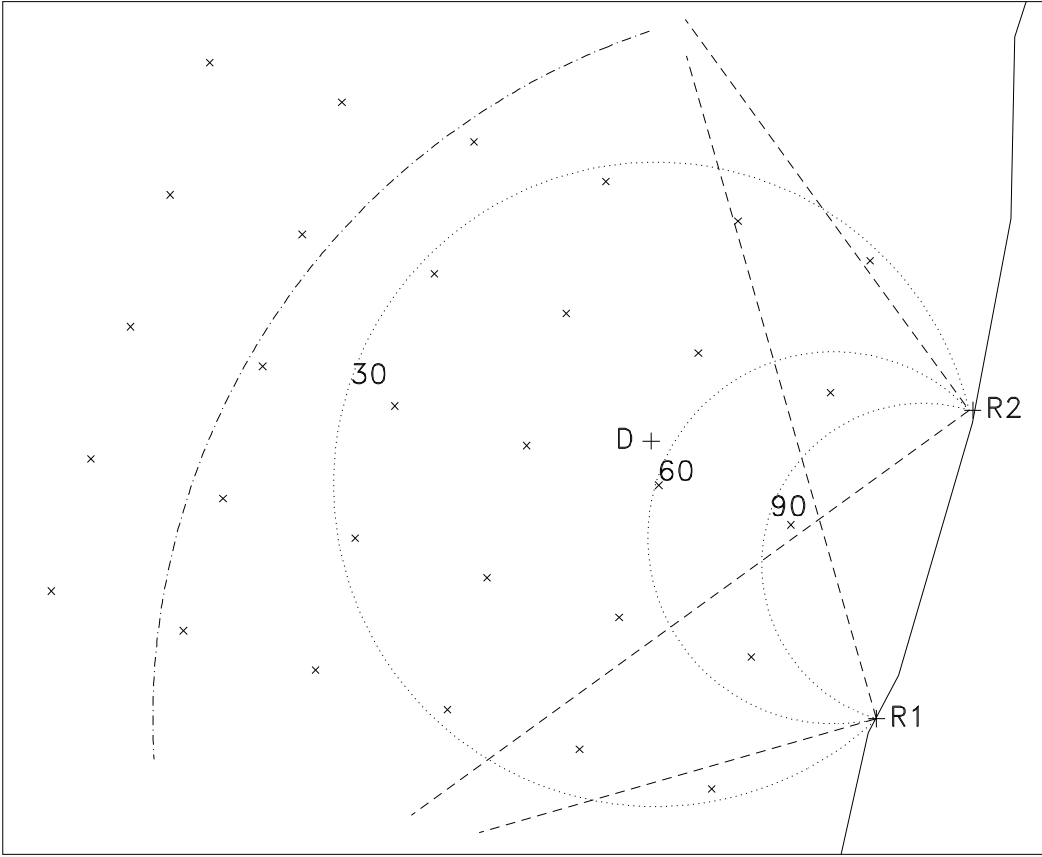


Figure 8

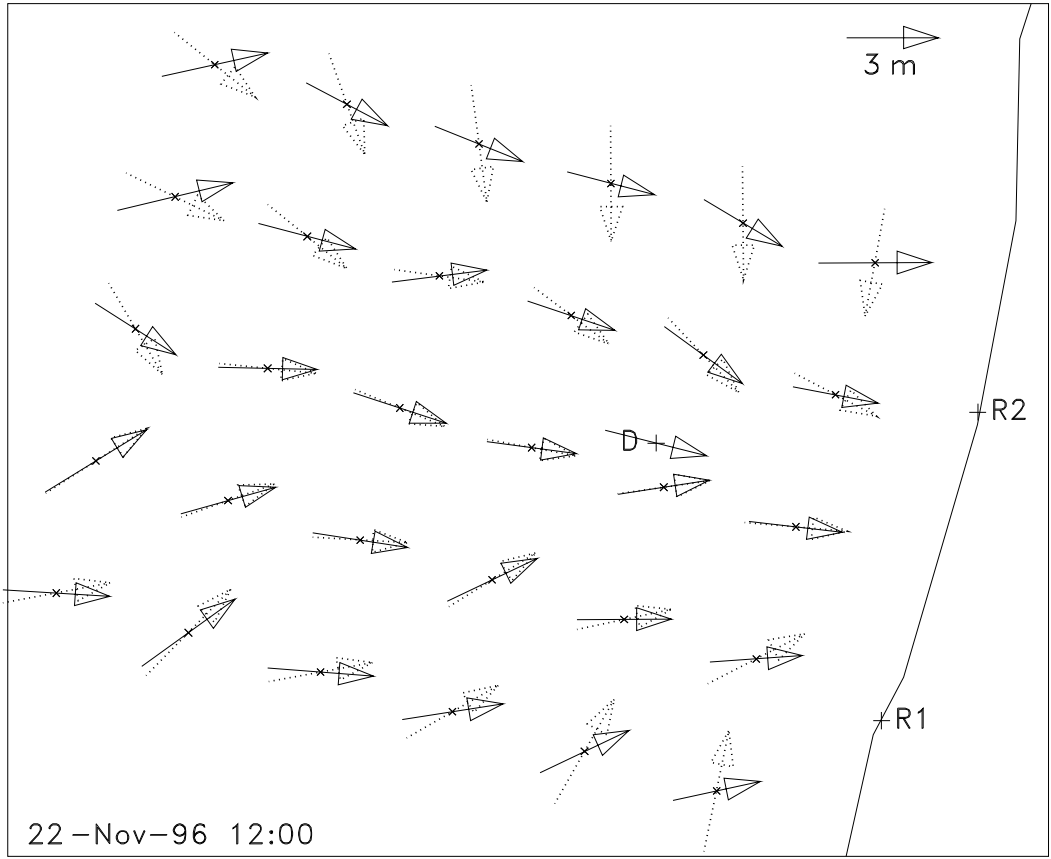


Figure 9

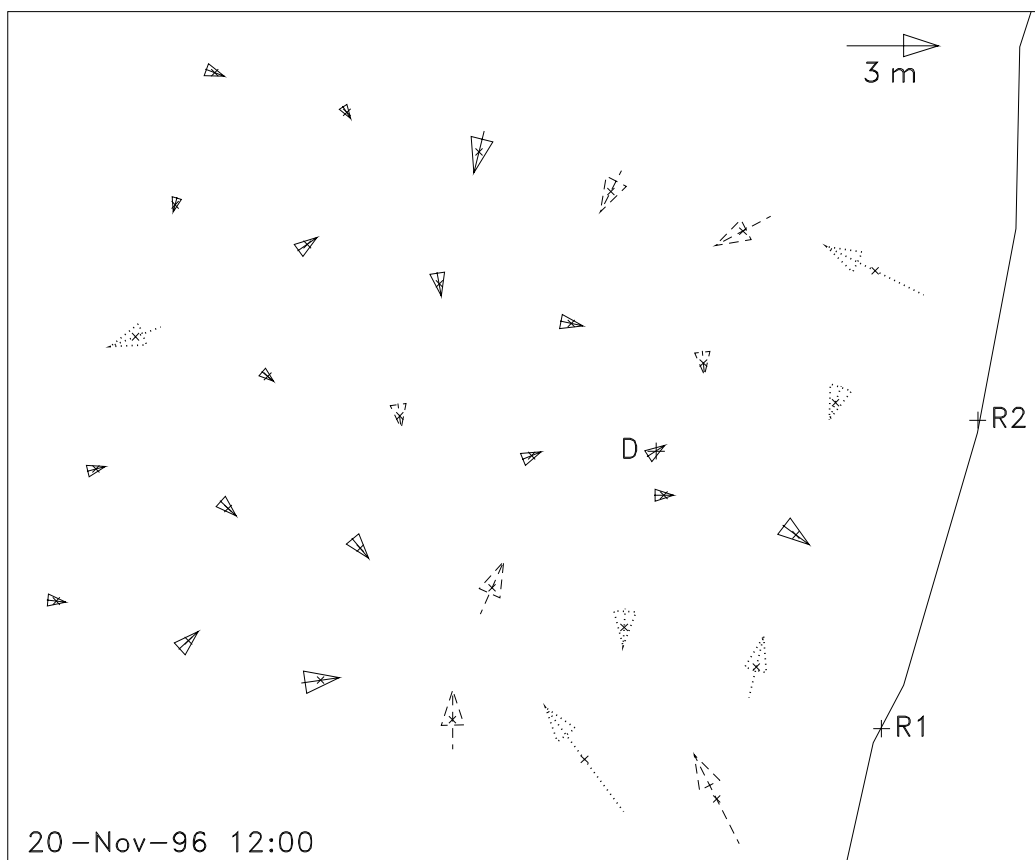


Figure 10